

Electric Polarization from Many-Body Neural Network Ansatz

Xiang Li,^{1,*} Yubing Qian,^{1,2,†} and Ji Chen^{2,3,‡}

¹ByteDance Research, Zhonghang Plaza, No. 43,
North 3rd Ring West Road, Haidian District, Beijing.

²School of Physics, Peking University, Beijing 100871, People's Republic of China

³Interdisciplinary Institute of Light-Element Quantum Materials,
Frontiers Science Center for Nano-Optoelectronics,

Peking University, Beijing 100871, People's Republic of China

(Dated: August 15, 2023)

Ab initio calculation of dielectric response with high-accuracy electronic structure methods is a long-standing problem, for which mean-field approaches are widely used and electron correlations are mostly treated via approximated functionals. Here we employ a neural network wavefunction ansatz combined with quantum Monte Carlo to incorporate correlations into polarization calculations. On a variety of systems, including isolated atoms, one-dimensional chains, two-dimensional slabs, and three-dimensional cubes, the calculated results outperform conventional density functional theory and are consistent with the most accurate calculations and experimental data. Furthermore, we have studied the out-of-plane dielectric constant of bilayer graphene using our method and re-established its thickness dependence. Overall, this approach provides a powerful tool to consider electron correlation in the modern theory of polarization.

Electric polarization plays a crucial role in electromagnetic phenomena such as ferroelectricity and piezoelectricity. Despite its significance, a proper microscopic definition of polarization was only formulated in the 1990s [1, 2], which revealed the hidden relation between physical polarization and the Berry phase of solid systems. This theoretical advance leads to successful calculations of the dielectric response of solid materials from first principles [3–5], which is critical in several fields of condensed matter physics, such as the ferroelectric and topological materials [6]. However, the underlying electronic structure methods are mostly mean-field approaches such as density functional theory (DFT) [7], which has its limitation because the result depends heavily on the so-called exchange-correlation functional. Exchange-correlation functionals can not fully account for the exact correlation effects of electrons. In particular, widely used semi-local functionals often produce an excessive overestimate of electric susceptibility [5, 8]. Although correlated wavefunction methods, such as coupled-cluster theory can also be employed to calculate polarization [9], their high computational complexity hinders their application in solid systems. Furthermore, most of these correlated electronic structure methods are limited in open boundary conditions (OBC) for polarization calculations, which leads to slow convergence and heavy computational costs towards the thermodynamic limit (TDL), see Fig. 1 for a summary of the state-of-the-art methods in polarization calculations.

In addition to the conventional deterministic electronic structure methods mentioned above, quantum Monte Carlo (QMC) methods are also widely adopted for elec-

tronic structure calculations, showing favorable computational scaling and high accuracy [10–12]. Pioneering works to study electric susceptibility using QMC have been reported [13, 14], in which traditional Slater Jastrow type wavefunction is combined with diffusion Monte Carlo (DMC) to study polarization of hydrogen chains in periodic boundary conditions (PBC). The main difficulty for DMC is to write down the local self-consistent Hamiltonian under a finite electric field and run calculations iteratively. Despite the promising results on hydrogen chain [13], there are still grand challenges: multiple loops of DMC are needed for the self-consistent procedure, a complex forward walking strategy is required for evaluat-

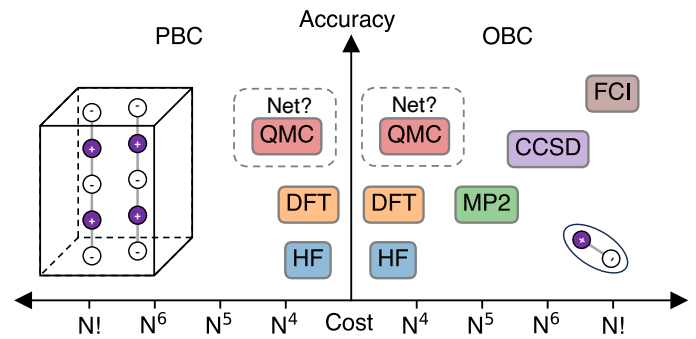


FIG. 1. A brief illustration of the computational cost and accuracy of different electronic structure methods in polarization calculations. N denotes the number of electrons in the system. High-level correlated wavefunction methods are not shown in the PBC panel because they have not been applied to PBC polarization calculations so far. QMC: quantum Monte Carlo; DFT: density functional theory; HF: Hartree-Fock; MP2: second-order Møller-Plesset perturbation theory; CCSD: coupled cluster with single and double excitations; FCI: full configuration interaction.

* lixiang.62770689@bytedance.com

† X. L. and Y. Q. contributed equally to this work.

‡ ji.chen@pku.edu.cn

ing the polarization, and the quality of trial wavefunction affects the accuracy of DMC. Therefore, it is desirable to develop more accurate and efficient approaches to calculate the electric polarization of solid systems.

In recent years, there has been significant progress in the application of neural network in the electronic structure community. Neural network wavefunction ansatz combined with QMC simulations has demonstrated higher accuracy with lower computational complexity than conventional high-order wavefunction methods [15–33]. The expressiveness of neural network overcomes the main bottleneck of traditional wavefunction ansatz in QMC, making the approach a competitive option for state-of-the-art electronic structure calculation. So far, the neural network QMC calculations have shown great power in treating spin systems [15–17], molecules [18–21], periodic models [25–28], and real solids [28, 29].

In this work, we extend the neural network QMC calculation to the electric polarization of solid systems. Specifically, we employ a recently developed solid neural network, dubbed DeepSolid [28], in conjunction with variational Monte Carlo (VMC). Antithetic sampling [34] is developed for efficient computation of the Berry phase and thus the electric polarization. Our approach has been tested on a diverse range of systems, including isolated atoms, one-dimensional chains, two-dimensional slabs, three-dimensional cubes, and bilayer graphene. The results demonstrate clear advantages of our approach over traditional methods.

To introduce our methodology, let us consider a crystal system under a finite electric field \mathbf{E} , the enthalpy of this system is formulated below [3, 4, 13, 37]

$$F[\psi] = \frac{\langle \psi | \hat{H}_S | \psi \rangle}{\langle \psi | \psi \rangle} - \Omega_S \mathbf{E} \cdot \mathbf{P}[\psi], \quad (1)$$

where \hat{H}_S denotes the supercell Hamiltonian in the absence of electric field \mathbf{E} , and Ω_S is the supercell volume. The term $-\Omega_S \mathbf{E} \cdot \mathbf{P}$ represents the interaction between electric polarization density \mathbf{P} and electric field. However, a proper microscopic definition of $\mathbf{P}[\psi]$ remains absent for decades since the ordinary position operator $\hat{\mathbf{r}}$ violates the periodic boundary condition. This problem was finally solved after recognizing the polarization as the Berry phase in the Brillouin zone, according to which the polarization can be extracted from a general wavefunction ψ as follows [38]

$$\mathbf{P}[\psi] = -\frac{1}{\Omega_S} \sum_i \frac{\mathbf{a}_i}{2\pi} \text{Im} \ln \frac{\langle \psi | \hat{U}_i | \psi \rangle}{\langle \psi | \psi \rangle}, \quad (2)$$

$$\hat{U}_i = \exp \left[\mathbf{i} \mathbf{b}_i \cdot \left(\sum_e \hat{\mathbf{r}}_e - \sum_I Z_I \mathbf{R}_I \right) \right],$$

where $\mathbf{a}_i, \mathbf{b}_i$ denote lattice and reciprocal lattice vectors of the supercell. \hat{U}_i serves as a periodic generalization of the position operator $\hat{\mathbf{r}}$ in solid systems and $\text{Im} \ln(x)$ is used to extract the Berry phase within x . Note that \hat{U}_i

is an intrinsic many-body operator which includes all the electron coordinates in the exponent. A charge-weighted sum of ion coordinates $Z_I \mathbf{R}_I$ is also included to achieve translation invariance of polarization.

With the enthalpy functional formulated above, traditional methods usually start with a Hartree-Fock (HF) ansatz, which is typically expressed as follows

$$\psi_{\text{HF}}(\mathbf{r}) = \text{Det} [e^{\mathbf{i} \mathbf{k}_i \cdot \mathbf{r}_j} u_{\mathbf{k}_i}(\mathbf{r}_j)]. \quad (3)$$

Electrons are treated independently of each other with a mean-field interaction in Eq. (3), simplifying quantum many-body problems but also deviating from the ground truth. To fully treat the electron correlation effects, we employ a correlated neural network wavefunction ψ_{net} from DeepSolid [28], whose general form reads

$$\psi_{\text{net}}(\mathbf{r}) = \text{Det} [e^{\mathbf{i} \mathbf{k}_i \cdot \mathbf{r}_j} u_{\mathbf{k}_i}(\mathbf{r}_j; \mathbf{r}_{\neq j})], \quad (4)$$

where $\mathbf{r}_{\neq j}$ denotes all the electron coordinates except \mathbf{r}_j . Eq. (4) resembles the form of the traditional Bloch function, while cell-periodic functions $u_{\mathbf{k}}$ are now represented using deep neural networks that rely on all electrons to accommodate electron correlations [19]. Electron features \mathbf{r}_i are converted to be periodic and permutation equivariant before being fed into neural networks, and complex-valued orbitals $u_{\mathbf{k}}$ are constructed with a pair of neural networks outputting the real and imaginary part respectively. As a result, Fermionic anti-symmetry, periodicity, and complex-valued nature are all encoded in our network, promoting it to be a legitimate and expressive ansatz for solid. See Ref. [28] for more details of the architecture.

Using the neural network we have constructed, the enthalpy functional outlined in Eq. (1) can be efficiently minimized through variational Monte Carlo, allowing for gradual convergence to the ground truth. However, there have been significant fluctuations observed in \hat{U}_i evaluation, which seriously impedes optimization. As a solution, antithetic sampling is employed in the Monte Carlo evaluation, which reads

$$\langle \hat{U}_i \rangle = \frac{\int d\mathbf{r} |\psi(\mathbf{r})|^2 U_i(\mathbf{r})}{\int d\mathbf{r} |\psi(\mathbf{r})|^2} = \frac{\int d\mathbf{r} |\psi(\mathbf{r})|^2 \tilde{U}_i(\mathbf{r})}{\int d\mathbf{r} |\psi(\mathbf{r})|^2}, \quad (5)$$

$$\tilde{U}_i(\mathbf{r}) = \frac{1}{2} \left[U_i(\mathbf{r}) + \frac{|\psi(-\mathbf{r})|^2}{|\psi(\mathbf{r})|^2} U_i(-\mathbf{r}) \right].$$

And thus the fluctuations are significantly reduced through the cancellation between $U_i(\mathbf{r})$ and its inverted image $U_i(-\mathbf{r})$. It's worth noting that centrosymmetric cells are assumed in Eq. (5), and one can choose other images for cancellation if central symmetry is not satisfied. To further improve efficiency, we have employed a Kronecker-factored curvature estimator (KFAC) optimizer [39], which effectively integrates second-order information into the optimization process, surpassing traditional optimizers. See the Supplementary Material for more computational details, and the code of this work is

TABLE I. Calculated atom polarizability in atomic unit (Bohr^3). DeepSolid results are labeled as DS. B3LYP, HF, and CCSD(T) results are calculated with PySCF [35] in the def2-qzvpvd basis set and non-relativistic limit. Recommended data is taken from Ref. [36], which is deduced from experiment data and the most accurate calculations.

	H	He	Li	Be	N	Ne	MAE
B3LYP	5.187	1.485	142.727	43.090	7.711	2.838	4.669
HF	4.484	1.318	169.231	45.441	7.138	2.365	2.243
CCSD(T)	4.484	1.372	165.803	37.707	7.212	2.642	0.326
DS	4.51	1.39	165.0	36.95	7.16	2.67	0.32
Recommended	4.5(exact)	1.38375(2)	164.1125(5)	37.74(3)	7.4(2)	2.66110(3)	0

developed at the open-source repository of DeepSolid ¹.

Isolated atoms are the first systems selected for direct comparison with the most accurate methods and experimental data. In our calculations, we place a single atom in a large enough box to eliminate periodic image interactions. The calculated polarizability α is shown in Tab. I, which measures the linear response of the dipole moment to the applied field and has some subtle relation with the bulk susceptibility χ (see Supplementary Material). Results from DFT with the B3LYP functional, HF, and CCSD(T) under OBC are also listed for comparison. P-state atoms (B, C, O, F) are skipped because their anisotropy requires special treatments [40]. As can be seen from Tab. I, although B3LYP is widely-trusted functional belonging to the fourth rung of the so-called Jacob’s ladder of DFT, it consistently deviates from the ground truth and has a relatively large mean absolute error (MAE). The behavior of DFT is due to the inaccuracy in treating the exchange-correlation effects, which can be very different for energy and polarization calculations. In HF calculations, because of the explicit treatment of non-local exchange, deviations in polarization are significantly reduced. CCSD(T) is the coupled cluster theory with single, double, and perturbative triple excitations, and is considered a very accurate method in the literature. It further incorporates correlation effects on top of HF wavefunction and achieves smaller MAE than HF results. Overall, DeepSolid results are comparable with CCSD(T), showing that the exchange-correlation treatments in our neural network are accurate and reliable for polarization calculations.

Having demonstrated our technique with single atoms, we proceed to simulate periodic systems by arranging bonded molecules into a one-dimensional chain and a two-dimensional slab. These systems are widely known as challenging cases for conventional DFT methods, which would have a serious overestimation of their longitudinal susceptibility. This problem stems from the fact that surface charges are insensitive to the bulk charge within the system when non-local interactions are absent, and this can be solved using more accurate *ab initio* methods [5]. For the one-dimensional case, hydrogen chain ($n \text{ H}_2$) and polyynes ($n \text{ C}_2$) are studied, and

the simulation size is pushed to 22 H_2 and 7 C_2 respectively for TDL convergence. Correlation-consistent effective core potential (ccECP) is employed for polyynes to accelerate neural network optimization and reduce fluctuation [31, 44]. The final results are plotted in Fig. 2, which show that susceptibility calculated by DeepSolid agrees well with correlated wavefunction methods CCSD(T) and random phase approximation (RPA). Local-density approximation (LDA) functional deviates severely from the ground truth for one-dimensional chains [9], but the use of hybrid functions such as B3LYP leads to partial recovery of non-local exchange effects and, consequently, a reduction in the overshoot. HF is much better than DFT calculations, which further proves the importance of the

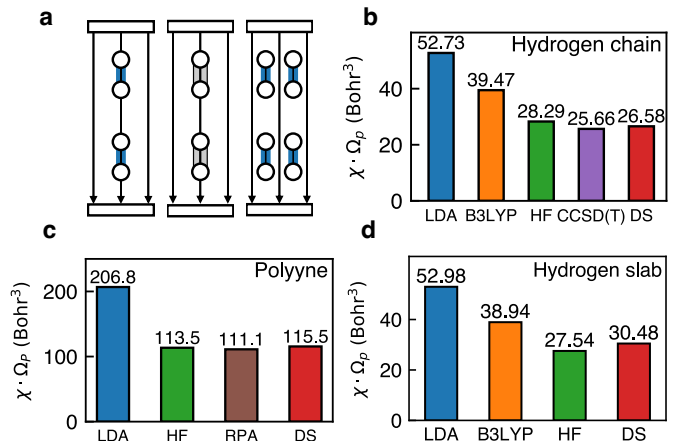


FIG. 2. Calculations of chains and slabs. DeepSolid results are labeled as DS. (a) illustrations of hydrogen chain, polyynes, hydrogen slab, and the applied electric field. (b) hydrogen chain, (c) polyynes, (d) hydrogen slab susceptibilities $\chi \cdot \Omega_p$ denotes the volume of the primitive cell. For the hydrogen system, LDA and HF results were calculated with the 3-21G basis set under PBC [5]. CCSD(T) calculations were performed with the 6-311G** basis set under OBC [9]. Intrapair and interpair distances are set to 2 and 3 Bohr respectively for the hydrogen chain. The interchain distance is set to 4.724 Bohr for the slab. For polyynes, the alternating distance between carbon atoms is set to 1.18 and 1.4 Å. LDA, HF, and RPA results were calculated with 6-31G, 3-21G, and 4-31G basis set respectively under OBC [41–43].

¹ <https://github.com/bytedance/DeepSolid>

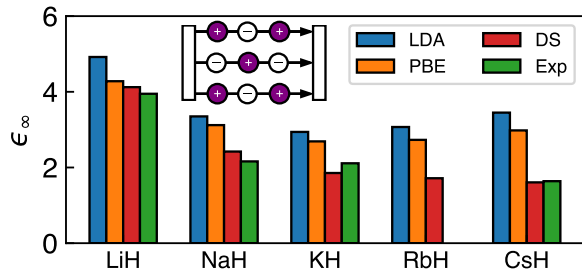


FIG. 3. Calculated high-frequency dielectric constant ϵ_∞ of alkali metal hydrides XH. DeepSolid results are labeled as DS. LDA and PBE results in PBC are taken from Ref. [45]. Experimental data are taken from Refs. [46–48], which are derived from refractive indexes n_D for sodium doublet (589.29 nm) via Eq. (6). RbH experiments are absent.

non-local exchange effect for electric polarization calculation in this system. As we arrange hydrogen chains periodically to form hydrogen slabs, the computational cost of high-level deterministic wavefunction methods, such as CCSD(T), grows rapidly and is soon beyond reach. However, our approach has a lower scaling and we can obtain the first accurate polarization calculation for such a hydrogen slab (Fig. 2d). And for the slab, the performances of DFT and HF compared with our accurate neural network results are similar to those observed for the chains.

To further test our method, we applied it to alkali metal hydrides and calculated their dielectric constants, allowing direct comparison with experimental results. These systems have a simple structure, consisting of alternating cations and anions, but they are of considerable research significance due to their relevance in hydrogen storage applications [49]. The high-frequency dielectric constant ϵ_∞ can be extracted through optical experiments from the following relations,

$$\begin{aligned} \mathbf{D} &= \epsilon_\infty \mathbf{E} = \mathbf{E} + 4\pi \mathbf{P}, \\ \epsilon_\infty &= 1 + 4\pi\chi = n_D^2, \end{aligned} \quad (6)$$

where n_D denotes the corresponding refractive index. In the visible light regime, ions are almost frozen relative to the incident light frequency and this leads to the dominance of electric polarization in ϵ_∞ . These three-dimensional systems are also qualitatively different from the chains and slabs, because the fluctuation of \hat{U}_i increases as we tile the cells in all three directions to form the simulation cell. To balance the influence from finite-size error and \hat{U}_i fluctuations, we tile the conventional cell in the direction of the applied field \mathbf{E} and the transverse directions remain unchanged. Moreover, Burkatzki-Filippi-Dolg (BFD) pseudopotential [50] is used to remove inertial core electrons [31]. Our calculations have been pushed to the $4 \times 1 \times 1$ supercell and the results are plotted in Fig. 3. LDA and Perdew–Burke–Ernzerhof (PBE) results are also plotted for comparison, while more

accurate conventional wavefunction methods are not applicable due to computational costs. As we can see, numerical simulations and experiments agree that ϵ_∞ decreases as the alkali metal atom becomes heavy, since ϵ_∞ is inversely proportional to the cell volume in Eq. (6). However, LDA and PBE functionals [51] tend to overestimate ϵ_∞ , and the error is largest in CsH. In contrast, our DeepSolid results agree well with the experiment for all systems, which manifests the capability of neural network wavefunction to capture non-local exchange and correlation effects.

After demonstrating the accuracy of our methods in previous sections, we now proceed to apply our method to bilayer graphene (BLG), an extensively studied 2D material system known for its rich electronic properties. Despite its fundamental importance, the precise value of the dielectric constant of BLG remains elusive and has been an important subject of both experimental and theoretical works [52, 53]. Specifically, theoretical calculations reported were either restricted to DFT level [52] or based on values calculated with monolayer graphene [53]. Here we use DeepSolid to directly calculate the out-of-plane dielectric constant ϵ_∞^\perp of bilayer graphene. 2×2 supercells containing monolayer and equilibrium AA-stacked bilayer graphene were used. The calculated monolayer polarizability equals $5.7(1) \text{ Bohr}^3$ and bilayer polarizability equals $11.6(1) \text{ Bohr}^3$, which agrees with the linear dependence of polarizability on the number of layers as shown in Ref. [52]. Based on this linear dependence and following Ref. [54], one can derive the expression of the out-of-plane dielectric constant as a function of the layer separation d (see Supplementary Material):

$$\epsilon_\infty^\perp(d) = \left(1 - \frac{2\pi\alpha_{\text{equil}}^{\text{BLG}}}{S \cdot d} \right)^{-1}, \quad (7)$$

where $S = 5.25 \text{ \AA}^2$ denotes the area of the primitive cell. Using the computed polarizability $\alpha_{\text{equil}}^{\text{BLG}}$, we can re-establish the relation of ϵ_∞^\perp , which is plotted in Fig. 4. To further check Eq. (7), we also calculate the polarizability of bilayer graphene at slightly larger (4 \AA) and smaller

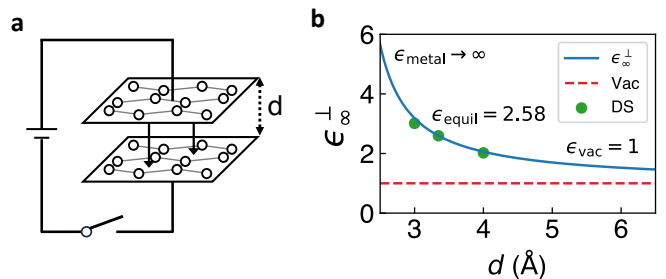


FIG. 4. Calculated effective 2D dielectric constant ϵ_∞^\perp of bilayer graphene. (a) plot of bilayer graphene under electric field. (b) calculated ϵ_∞^\perp as a function of graphene layer distance d . The equilibrium separation of BLG is set to 3.347 \AA .

(3Å) layer distances and plot the corresponding dielectric constant in Fig. 4, and the results agrees well with each other. Moreover, there are two notable limits when varying the layer separation d : as d decreases, two graphene layers coincide with each other and the system becomes metallic, which explains the diverging of $\epsilon_{\infty}^{\perp}$; as d becomes large, BLG polarization becomes negligible and vacuum contribution dominants in $\epsilon_{\infty}^{\perp}$ which approaches unity. The thickness-dependent dielectric constant will be valuable for further understanding and tuning the stacked multilayer graphene systems.

In conclusion, this work proposes an efficient and accurate method for investigating solid polarization based on the recently developed solid neural network wavefunction combined with quantum Monte Carlo. Our approach demonstrates superiority over the conventional state-of-the-art electronic structure methods. In the future, with

the proposed framework, it is promising to investigate a wide range of phenomena, including ferroelectricity, topological electronic transport, quantum Hall effect, and orbital magnetization, among others, on a higher level of accuracy and with electron correlations accounted for properly. Furthermore, this work provides more possibilities for utilizing neural network applications in condensed matter physics.

ACKNOWLEDGEMENTS

We want to thank ByteDance Research Group for inspiration and encouragement. This work is directed and supported by Hang Li and ByteDance Research. J.C. is supported by the National Natural Science Foundation of China under Grant No. 92165101.

-
- [1] R. D. King-Smith and D. Vanderbilt, Theory of polarization of crystalline solids, *Physical Review B* **47**, 1651 (1993).
 - [2] R. Resta, Macroscopic polarization in crystalline dielectrics: The geometric phase approach, *Reviews of Modern Physics* **66**, 899 (1994).
 - [3] R. W. Nunes and X. Gonze, Berry-phase treatment of the homogeneous electric field perturbation in insulators, *Physical Review B* **63**, 155107 (2001).
 - [4] I. Souza, J. Íñiguez, and D. Vanderbilt, First-Principles Approach to Insulators in Finite Electric Fields, *Physical Review Letters* **89**, 117602 (2002).
 - [5] B. Kirtman, V. Lacivita, R. Dovesi, and H. Reis, Electric field polarization in conventional density functional theory: From quasilinear to two-dimensional and three-dimensional extended systems, *The Journal of chemical physics* **135**, 154101 (2011).
 - [6] D. Xiao, M.-C. Chang, and Q. Niu, Berry phase effects on electronic properties, *Rev. Mod. Phys.* **82**, 1959 (2010).
 - [7] W. Kohn, Nobel lecture: Electronic structure of matter—wave functions and density functionals, *Rev. Mod. Phys.* **71**, 1253 (1999).
 - [8] M. van Faassen, P. L. de Boeij, R. van Leeuwen, J. A. Berger, and J. G. Snijders, Ultranonlocality in time-dependent current-density-functional theory: Application to conjugated polymers, *Phys. Rev. Lett.* **88**, 186401 (2002).
 - [9] B. Champagne, D. H. Mosley, M. Vračko, and J.-M. André, Electron-correlation effects on the static longitudinal polarizability of polymeric chains. ii. bond-length-alternation effects, *Phys. Rev. A* **52**, 1039 (1995).
 - [10] D. M. Ceperley and B. J. Alder, Ground state of the electron gas by a stochastic method, *Phys. Rev. Lett.* **45**, 566 (1980).
 - [11] W. M. C. Foulkes, L. Mitas, R. J. Needs, and G. Rajagopal, Quantum monte carlo simulations of solids, *Rev. Mod. Phys.* **73**, 33 (2001).
 - [12] G. H. Booth, A. Grüneis, G. Kresse, and A. Alavi, Towards an exact description of electronic wavefunctions in real solids, *Nature* **493**, 365 (2013).
 - [13] P. Umari, A. J. Williamson, G. Galli, and N. Marzari, Dielectric response of periodic systems from quantum monte carlo calculations, *Phys. Rev. Lett.* **95**, 207602 (2005).
 - [14] P. Umari and N. Marzari, Linear and nonlinear susceptibilities from diffusion quantum Monte Carlo: Application to periodic hydrogen chains, *The Journal of Chemical Physics* **131**, 094104 (2009).
 - [15] G. Carleo and M. Troyer, Solving the quantum many-body problem with artificial neural networks, *Science* **355**, 602 (2017).
 - [16] Y. Nomura, A. S. Darmawan, Y. Yamaji, and M. Imada, Restricted Boltzmann machine learning for solving strongly correlated quantum systems, *Physical Review B* **96**, 205152 (2017).
 - [17] G. Carleo, Y. Nomura, and M. Imada, Constructing exact representations of quantum many-body systems with deep neural networks, *Nature Communications* **9**, 1 (2018).
 - [18] J. Han, L. Zhang, and E. Weinan, Solving many-electron schrödinger equation using deep neural networks, *Journal of Computational Physics* **399**, 108929 (2019).
 - [19] D. Pfau, J. Spencer, A. de G. Matthews, and W. Foulkes, Ab-initio solution of the many-electron schrödinger equation with deep neural networks, *Phys. Rev. Research* **2**, 033429 (2020).
 - [20] J. Hermann, Z. Schätzle, and F. Noé, Deep-neural-network solution of the electronic schrödinger equation, *Nature Chemistry* **12**, 891 (2020).
 - [21] K. Choo, A. Mezzacapo, and G. Carleo, Fermionic neural-network states for ab-initio electronic structure, *Nature communications* **11**, 2368 (2020).
 - [22] M. Entwistle, Z. Schätzle, P. A. Erdman, J. Hermann, and F. Noé, Electronic excited states in deep variational monte carlo, *Nature Communications* **14**, 274 (2023).
 - [23] M. Entwistle, Z. Schätzle, P. A. Erdman, J. Hermann, and F. Noé, Electronic excited states in deep variational monte carlo, *Nature Communications* **14**, 274 (2023).
 - [24] J. Hermann, J. Spencer, K. Choo, A. Mezzacapo, W. Foulkes, D. Pfau, G. Carleo, and F. Noé, Ab-initio quantum chemistry with neural-network wavefunctions,

- arXiv preprint arXiv:2208.12590 (2022).
- [25] M. Wilson, S. Moroni, M. Holzmann, N. Gao, F. Wudarski, T. Vegge, and A. Bhowmik, Neural network ansatz for periodic wave functions and the homogeneous electron gas, *Phys. Rev. B* **107**, 235139 (2023).
- [26] G. Cassella, H. Sutterud, S. Azadi, N. Drummond, D. Pfau, J. S. Spencer, and W. M. C. Foulkes, Discovering quantum phase transitions with fermionic neural networks, *Physical Review Letters* **130**, 036401 (2023).
- [27] G. Pescia, J. Han, A. Lovato, J. Lu, and G. Carleo, Neural-network quantum states for periodic systems in continuous space, *Physical Review Research* **4**, 023138 (2022).
- [28] X. Li, Z. Li, and J. Chen, Ab initio calculation of real solids via neural network ansatz, *Nature Communications* **13**, 7895 (2022).
- [29] N. Yoshioka, W. Mizukami, and F. Nori, Solving quasi-particle band spectra of real solids using neural-network quantum states, *Communications Physics* **4**, 106 (2021).
- [30] Y. Qian, W. Fu, W. Ren, and J. Chen, Interatomic force from neural network based variational quantum monte carlo, *The Journal of Chemical Physics* **157**, 164104 (2022).
- [31] X. Li, C. Fan, W. Ren, and J. Chen, Fermionic neural network with effective core potential, *Phys. Rev. Res.* **4**, 013021 (2022).
- [32] W. Ren, W. Fu, X. Wu, and J. Chen, Towards the ground state of molecules via diffusion monte carlo on neural networks, *Nature Communications* **14**, 1860 (2023).
- [33] H. Xie, Z.-H. Li, H. Wang, L. Zhang, and L. Wang, A deep variational free energy approach to dense hydrogen, arXiv preprint arXiv:2209.06095 (2022).
- [34] C. P. Robert and G. Casella, Controlling Monte Carlo Variance, in *Monte Carlo Statistical Methods*, Springer Texts in Statistics, edited by C. P. Robert and G. Casella (Springer, New York, NY, 2004) pp. 123–156.
- [35] Q. Sun, T. C. Berkelbach, N. S. Blunt, G. H. Booth, S. Guo, Z. Li, J. Liu, J. D. McClain, E. R. Sayfutyarova, S. Sharma, *et al.*, Pyscf: the python-based simulations of chemistry framework, *Wiley Interdisciplinary Reviews: Computational Molecular Science* **8**, e1340 (2018).
- [36] P. Schwerdtfeger and J. K. Nagle, 2018 table of static dipole polarizabilities of the neutral elements in the periodic table, *Molecular Physics* **117**, 1200 (2019).
- [37] R. W. Nunes and D. Vanderbilt, Real-Space Approach to Calculation of Electric Polarization and Dielectric Constants, *Physical Review Letters* **73**, 712 (1994).
- [38] R. Resta, Quantum-Mechanical Position Operator in Extended Systems, *Physical Review Letters* **80**, 1800 (1998).
- [39] J. Martens and R. Grosse, Optimizing neural networks with kronecker-factored approximate curvature, in *International conference on machine learning* (PMLR, 2015) pp. 2408–2417.
- [40] A. K. Das and A. J. Thakkar, Static response properties of second-period atoms: Coupled cluster calculations, *Journal of Physics B: Atomic, Molecular and Optical Physics* **31**, 2215 (1998).
- [41] M. A. Watson, P. Salek, P. Macak, and T. Helgaker, Linear-scaling formation of kohn-sham hamiltonian: Application to the calculation of excitation energies and polarizabilities of large molecular systems, *The Journal of chemical physics* **121**, 2915 (2004).
- [42] E. F. Archibong and A. J. Thakkar, Chain length dependence of static longitudinal polarizabilities and hyperpolarizabilities in linear polyynes, *The Journal of chemical physics* **98**, 8324 (1993).
- [43] E. K. Dalskov, J. Oddershede, and D. M. Bishop, Static and dynamic polarizability calculations for the polyyne series ($c_{2n}h_2$) with extrapolation to the infinite chain, *The Journal of chemical physics* **108**, 2152 (1998).
- [44] A. Annaberdiyev, C. A. Melton, M. C. Bennett, G. Wang, and L. Mitas, Accurate atomic correlation and total energies for correlation consistent effective core potentials, *Journal of Chemical Theory and Computation* **16**, 1482 (2020).
- [45] G. Barrera, D. Colognesi, P. Mitchell, and A. Ramirez-Cuesta, Lda or gga? a combined experimental inelastic neutron scattering and ab initio lattice dynamics study of alkali metal hydrides, *Chemical Physics* **317**, 119 (2005), combining Simulations and Neutron Scattering Experiments: from Models to Systems of Biological and Technological Interest.
- [46] E. Staritzky and D. I. Walker, Crystallographic data. 124. lithium hydride, lih; 125. lithium deuteride, lid, *Analytical Chemistry* **28**, 1055 (1956).
- [47] K. Ghandehari, H. Luo, A. L. Ruoff, S. S. Trail, and F. J. DiSalvo, Band gap and index of refraction of csh to 251 gpa, *Solid state communications* **95**, 385 (1995).
- [48] S. S. Batsanov, E. D. Ruchkin, and I. A. Poroshina, *Refractive indices of Solids* (Springer, 2016).
- [49] N. Rusman and M. Dahari, A review on the current progress of metal hydrides material for solid-state hydrogen storage applications, *International Journal of Hydrogen Energy* **41**, 12108 (2016).
- [50] M. Burkatzki, C. Filippi, and M. Dolg, Energy-consistent pseudopotentials for quantum Monte Carlo calculations, *The Journal of Chemical Physics* **126** (2007).
- [51] J. P. Perdew, K. Burke, and M. Ernzerhof, Generalized gradient approximation made simple, *Phys. Rev. Lett.* **77**, 3865 (1996).
- [52] E. Yu, D. Stewart, and S. Tiwari, Ab initio study of polarizability and induced charge densities in multilayer graphene films, *Physical Review B* **77**, 195406 (2008).
- [53] S. Slizovskiy, A. Garcia-Ruiz, A. I. Berdyugin, N. Xin, T. Taniguchi, K. Watanabe, A. K. Geim, N. D. Drummond, and V. I. Fal'ko, Out-of-plane dielectric susceptibility of graphene in twistrionic and bernal bilayers, *Nano Letters* **21**, 6678 (2021).
- [54] A. Laturia, M. L. Van de Put, and W. G. Vandenberghe, Dielectric properties of hexagonal boron nitride and transition metal dichalcogenides: from monolayer to bulk, *npj 2D Materials and Applications* **2**, 6 (2018).

SUPPLEMENTARY MATERIAL

I. GRADIENT FORMULA

DeepSolid ansatz can be straightforwardly optimized via enthalpy minimization, and the gradient reads

$$\begin{aligned}\nabla_{\theta}\langle F \rangle &= \mathbf{G}_1 + \mathbf{G}_2, \\ \mathbf{G}_1 &= \text{Re} \left[\langle \hat{H}_S \nabla_{\theta} \ln \psi^* \rangle - \langle \hat{H}_S \rangle \langle \nabla_{\theta} \ln \psi^* \rangle \right], \\ \mathbf{G}_2 &= \mathbf{E} \cdot \sum_i \frac{\mathbf{a}_i}{2\pi} \text{Re} \left[\left\langle \text{Im} \left[\frac{\hat{U}_i}{\langle \hat{U}_i \rangle} \right] \nabla_{\theta} \ln \psi^* \right\rangle \right].\end{aligned}\quad (1)$$

Note that antithetic sampling is used in $\langle \hat{U}_i \rangle$ evaluation.

II. QUANTITY DEFINITION

The electric susceptibility of materials is defined as

$$\chi = \left. \frac{\partial \mathbf{P}}{\partial \mathbf{E}} \right|_{\mathbf{E}=0}, \quad (2)$$

where \mathbf{E} is the macroscopic electric field in the medium. Polarizability for isolated atoms and molecules is defined as

$$\alpha = \left. \frac{\partial \mathbf{p}}{\partial \mathbf{E}_{\text{ext}}} \right|_{\mathbf{E}_{\text{ext}}=0}, \quad (3)$$

where \mathbf{p} is the induced dipole moment and \mathbf{E}_{ext} denotes the external electric field. Despite the difference, the enthalpy formula is still applicable for isolated atoms, simply by replacing $\Omega_S \mathbf{P}$ with \mathbf{p} and \mathbf{E} with \mathbf{E}_{ext} .

It's worth noting that susceptibility or polarizability receives non-linear contribution under finite electric fields, which reads

$$\left. \frac{\partial \mathbf{p}}{\partial \mathbf{E}_{\text{ext}}} \right|_{\mathbf{E}_{\text{ext}}} = \alpha + \frac{1}{6} \gamma \mathbf{E}_{\text{ext}}^2, \quad (4)$$

where γ denotes the hyperpolarizability of the system and higher order term are omitted. The applied electric fields should be small enough to neglect non-linear contribution.

Isolated slab polarizability is related to susceptibility χ as follows [1]

$$\alpha_{\text{slab}} = \Omega_p \frac{\chi}{1 + 4\pi\chi} = \frac{\Omega_p}{4\pi} \left(1 - \frac{1}{\epsilon_{\text{SC}}^{\perp}} \right), \quad (5)$$

where $\epsilon_{\text{SC}}^{\perp}$ denotes the dielectric constant of supercell perpendicular to the slab. $\epsilon_{\text{SC}}^{\perp}$ received contributions from vacuum and contained 2D slab, which can be formulated as below [2]

$$\frac{c}{\epsilon_{\text{SC}}^{\perp}} = \frac{c-t}{\epsilon_{\text{vac}}} + \frac{t}{\epsilon_{\text{2D}}^{\perp}}, \quad (6)$$

where c denotes the perpendicular length of supercell and t denotes the thickness of 2D material. The effective dielectric constant $\epsilon_{\text{2D}}^{\perp}$ of 2D material can then be derived

$$\epsilon_{\text{2D}}^{\perp} = \left[1 + \frac{c}{t} \left(\frac{1}{\epsilon_{\text{SC}}^{\perp}} - 1 \right) \right]^{-1} = \left(1 - \frac{4\pi\alpha_{\text{slab}}}{A \cdot t} \right)^{-1}, \quad (7)$$

where A denotes the unit area of primitive cell. For bilayer material, $t = 2d$ and d denotes the layer distance.

TABLE I. Recommended hyperparameters

Hyperparameter	Value	Hyperparameter	Value
Pretrain basis	NA	Pretrain iterations	NA
Dimension of one-electron layer \mathbf{V}	256	Dimension of two-electron layer \mathbf{W}	32
Number of layers	4	Number of determinants	8
Optimizer	KFAC	Learning rate	1e-2
Learning rate decay	2	Learning rate delay	1e4
Damping	1e-3	Constrained norm of gradient	1e-3
Momentum of optimizer	0.0	Batch size	4096
Number of training steps	1e5	Clipping window of gradient	5
MCMC burn in	1e3	MCMC steps between each iteration	30
MCMC move width	2e-2	Target MCMC acceptance	55%
Precision	Float64	Number of inference steps	2e4

III. HYPERPARAMETERS

The specific architecture of the neural network can be seen in Ref. [3], and hyperparameters used in simulations are listed in Tab. I. The main difference from previous studies is the enlarged learning rate decay, which affects the learning rate as follows

$$\text{lr}_i = \frac{\text{lr}_0}{(1 + i/\text{delay})^{\text{decay}}}, \quad (8)$$

where lr denotes the learning rate, and i counts the training steps. Learning rate decay is enlarged to stabilize the train since polarizability α and susceptibility χ appear sensitive to fluctuations, smaller lr has the nearly same results with larger fluctuations in training. Part of the hyperparameters are different for test systems and will be clarified respectively. Moreover, Float64 is necessary for antithetic sampling.

IV. ATOMS

Single atoms are placed in a cubic cell with a length of 2000 Bohr to neglect image interactions. The applied electric fields are given in Tab. II. According to the hyperpolarizability calculated in Refs. [4–8] and Eq. (4), non-linear contributions to polarizability α caused by applied electric field are less than 0.01 Bohr³. Moreover, a larger learning rate (1e-1) and gradient clip window (10) are necessary to reach the energy minimum of lithium and beryllium. The training curves of polarizability are given in Fig. 1.

TABLE II. Applied electric field \mathbf{E} for atoms in atomic unit.

	H	He	Li	Be	N	Ne
\mathbf{E}	5e-3	1e-2	1e-3	2e-3	5e-3	1e-2

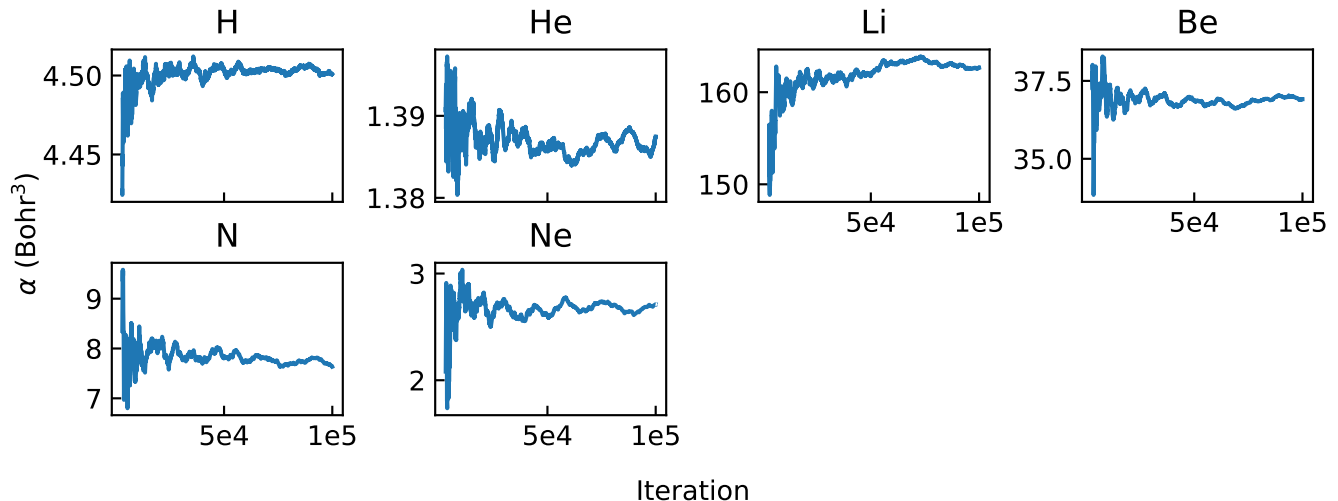


FIG. 1. Training curves of atom polarizabilities. For clarity, at each iteration number, we plot the median value of the last 10% of the corresponding iteration.

V. HYDROGEN CHAIN

Hydrogen chain geometry is set to be centrosymmetric for antithetic sampling, and it is given in Tab. III. The applied field is set to 1e-3 atomic unit. According to the hypersusceptibility calculated in Ref. [9], non-linear contributions to susceptibility caused by finite electric field are less than 0.01 Bohr³. Simulation size ranges from 10 H₂ to 22 H₂ to ensure TDL convergence and corresponding susceptibility χ is given in Tab. IV. The training curves of susceptibility are given in Fig. 2.

TABLE III. Geometry of hydrogen chain.

Atom	Position (Bohr)	Lattice vector	Value (Bohr)
H1	(1.5, 0, 0)	\mathbf{a}_1	(5, 0, 0)
H2	(3.5, 0, 0)	\mathbf{a}_2	(0, 100, 0)
		\mathbf{a}_3	(0, 0, 100)

TABLE IV. Longitudinal linear susceptibility of hydrogen chain.

System	10 H ₂	16 H ₂	22 H ₂
$\chi \cdot \Omega_p$ (Bohr ³)	25.21(1)	27.37(2)	26.58(2)

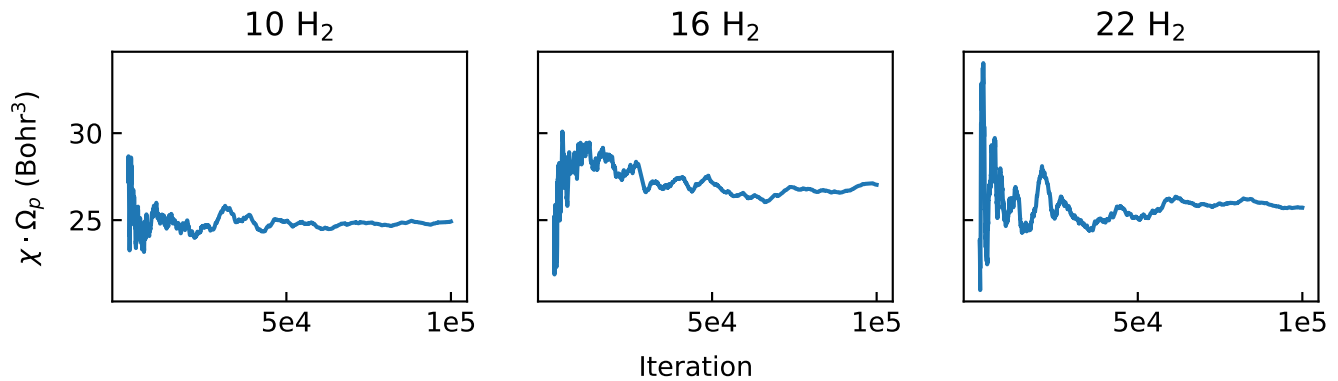


FIG. 2. Training curves of hydrogen chain susceptibilities. For clarity, at each iteration number, we plot the median value of the last 10% of the corresponding iteration.

VI. HYDROGEN SLAB

The specific geometry of the hydrogen slab is given in Tab. V. The applied field is set to $2e-3$ atomic unit. According to the hypersusceptibility calculated in Ref. [9], non-linear contributions caused by applied electric field are less than 0.04 Bohr^3 . Simulation size ranges from $2 \times 2 \text{ H}_2$ to $6 \times 6 \text{ H}_2$ to ensure TDL convergence and corresponding susceptibility χ is given in Tab. VI. The training curves of susceptibility is given in Fig. 3.

TABLE V. Geometry of hydrogen slab.

Atom	Position (Bohr)	Lattice vector	Value (Bohr)
H1	(1.5, 0, 0)	\mathbf{a}_1	(5, 0, 0)
H2	(3.5, 0, 0)	\mathbf{a}_2	(0, 4.724, 0)
		\mathbf{a}_3	(0, 0, 100)

TABLE VI. Susceptibility of hydrogen slab.

System	$2 \times 2 \text{ H}_2$	$4 \times 4 \text{ H}_2$	$6 \times 6 \text{ H}_2$
$\chi \cdot \Omega_p \text{ (Bohr}^3\text{)}$	20.44(1)	28.76(8)	30.5(2)

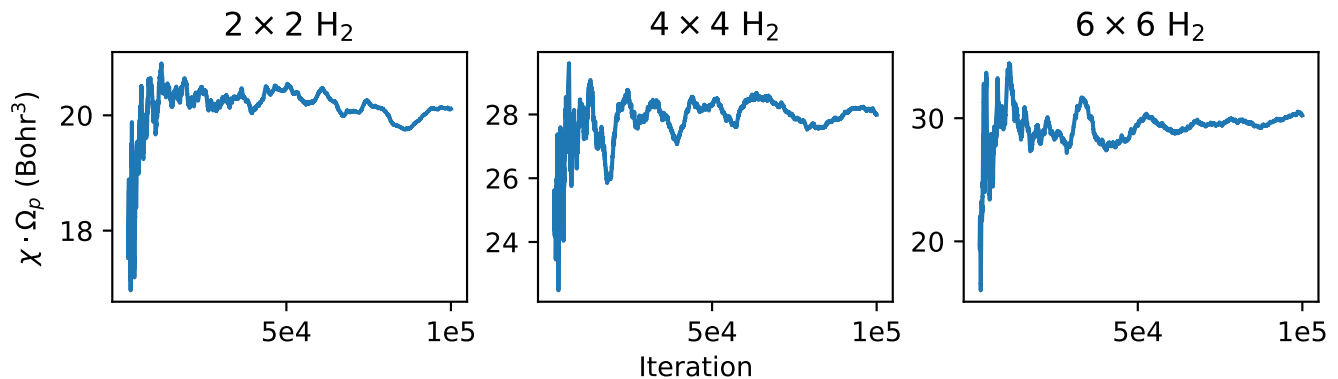


FIG. 3. Training curves of hydrogen slab susceptibilities. For clarity, at each iteration number, we plot the median value of the last 10% of the corresponding iteration.

VII. POLYNYNE

Polyyne n C_2 geometry is given in Tab. VII. The applied field is set to $1e-3$ atomic unit. According to the hypersusceptibility calculated in Ref. [10], non-linear contributions caused by applied electric field are less than 0.2 Bohr^3 . Simulation size is pushed to $n = 7$ and corresponding susceptibility χ is given in Tab. IV. The training curves of susceptibility are given in Fig. 4.

TABLE VII. Geometry of polyyne.

Atom	Position (\AA)	Lattice vector	Value (\AA)
C1	(0.7, 0, 0)	\mathbf{a}_1	(2.58, 0, 0)
C2	(1.88, 0, 0)	\mathbf{a}_2	(0, 100, 0)
		\mathbf{a}_3	(0, 0, 100)

TABLE VIII. Longitudinal linear susceptibility of polyyne.

System	5 C_2	7 C_2
$\chi \cdot \Omega_p$ (Bohr^3)	125.6(6)	115.5(3)

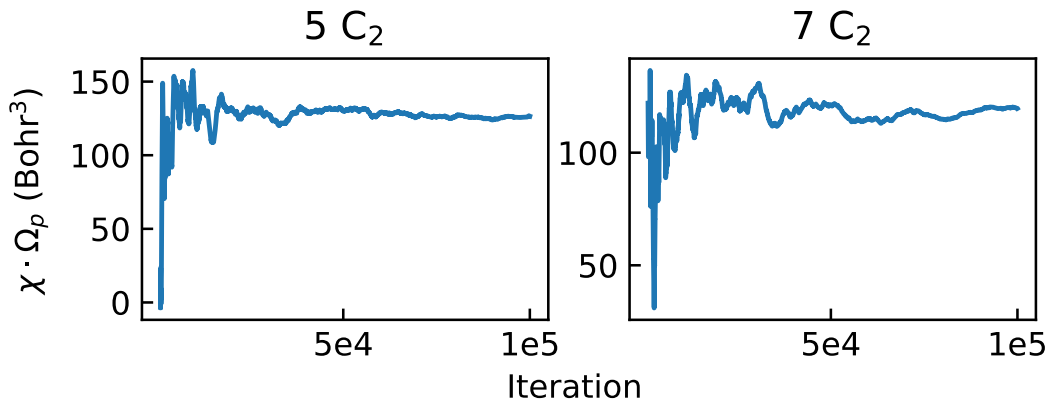


FIG. 4. Training curves of polyyne susceptibilities. For clarity, at each iteration number, we plot the median value of the last 10% of the corresponding iteration.

VIII. ALKALI METAL HYDRIDES

The specific geometry of alkali metal hydrides is given in Tab. IX. The lattice constant of each alkali metal is set to experiment data [11] and is given in Tab. X, the corresponding applied electric field is also listed. Smaller electric field ($2e-3$ atomic unit) is also used to check finite field effect, and nonlinear contribution is less than 0.1 Bohr^3 in susceptibility. High-frequency dielectric constants ϵ_∞ from DFT [11], DeepSolid(DS), and experiments [12–14] are given in Tab. XI. The training curves of high-frequency dielectric constant ϵ_∞ are given in Fig. 5. To ensure the TDL convergence, ϵ_∞ at different simulation sizes are given in Tab. XII.

TABLE IX. Geometry of alkali metal hydrides.

Atom	Position	Lattice vector	Position
H1	(L/2, 0, 0)	\mathbf{a}_1	(L, 0, 0)
H2	(0, L/2, 0)	\mathbf{a}_2	(0, L, 0)
H3	(0, 0, L/2)	\mathbf{a}_3	(0, 0, L)
H4	(L/2, L/2, L/2)		
X1	(0, 0, 0)		
X2	(0, L/2, L/2)		
X3	(L/2, 0, L/2)		
X4	(L/2, L/2, 0)		

TABLE X. Lattice constant and applied electric field \mathbf{E} of alkali metal hydrides.

XH	LiH	NaH	KH	RbH	CsH
L(\AA)	4.086	4.89	5.704	6.037	6.388
\mathbf{E}	5e-3	5e-3	5e-3	5e-3	5e-3

TABLE XI. High-frequency dielectric constant ϵ_∞ of alkali metal hydrides.

system	LiH	NaH	KH	RbH	CsH
LDA	4.92	3.35	2.94	3.07	3.45
PBE	4.28	3.12	2.69	2.73	2.98
DS	4.128(3)	2.422(1)	1.8546(6)	1.7162(4)	1.607(1)
Exp	3.939	2.161	2.111	NA	1.638

TABLE XII. High-frequency dielectric constant ϵ_∞ of alkali metal hydrides at different size.

ϵ_∞	$2 \times 1 \times 1$	$3 \times 1 \times 1$	$4 \times 1 \times 1$
LiH	3.913(3)	4.059(2)	4.128(3)
NaH	2.513(1)	2.447(1)	2.422(1)
KH	1.8951(5)	1.8419(5)	1.845(1)
RbH	1.7919(4)	1.7315(4)	1.7162(4)
CsH	1.6537(4)	1.6156(4)	1.607(1)

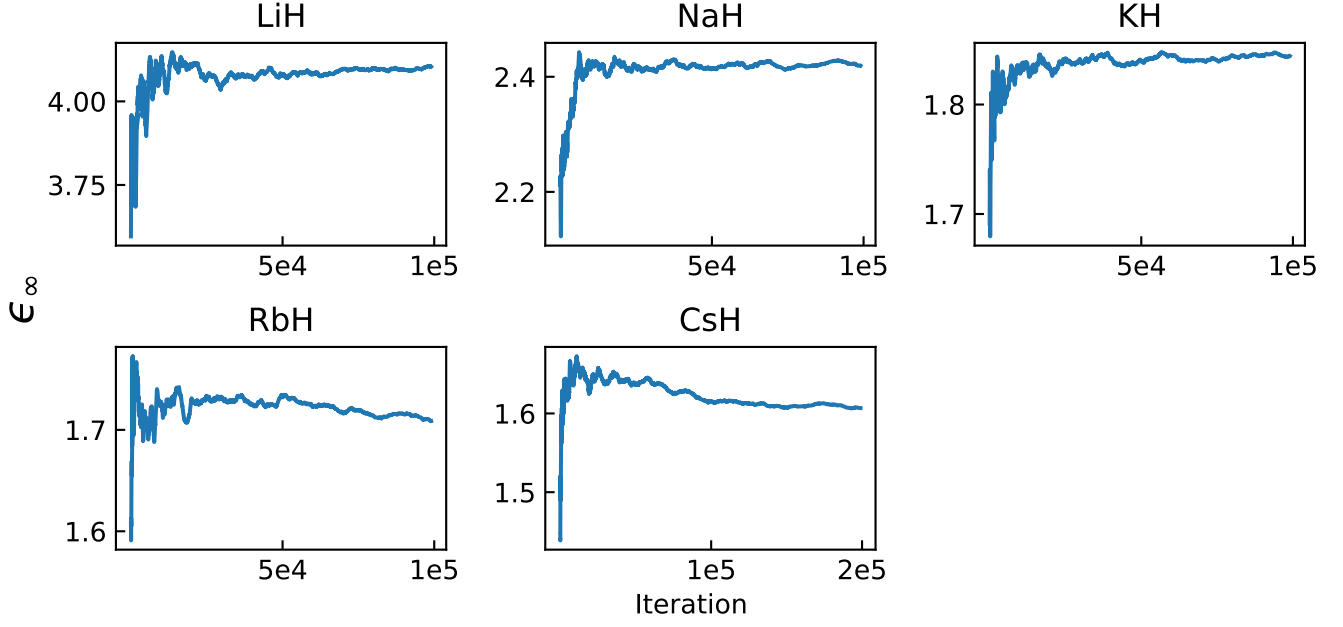


FIG. 5. Training curves of alkali metal hydrides dielectric constant ϵ_∞ . For clarity, at each iteration number, we plot the median value of the last 10% of the corresponding iteration.

IX. MONOLAYER GRAPHENE

Geometry of monolayer graphene is given in Tab XIII. Applied electric field is set to $5e-3$ atomic unit. Smaller electric field ($2e-3$ atomic unit) is also used to check finite field effect, and nonlinear contribution is less than 0.1 Bohr^3 in slab polarizability. Twist average is used to reduce finite size error and the formula reads

$$\alpha_{\text{avg}} = \frac{1}{9}\alpha_{\mathbf{k}_1} + \frac{2}{3}\alpha_{\mathbf{k}_2} + \frac{2}{9}\alpha_{\mathbf{k}_3}, \quad (9)$$

$$\mathbf{k}_1 = 0, \quad \mathbf{k}_2 = \frac{1}{3}\mathbf{b}_1 + \frac{1}{3}\mathbf{b}_2, \quad \mathbf{k}_3 = \frac{2}{3}\mathbf{b}_1 + \frac{1}{3}\mathbf{b}_2.$$

Corresponding training curve of polarizability α_\perp is given in Fig. 6. Final results is given in Tab. XIV.

TABLE XIII. Geometry of monolayer graphene.

Atom	Position (\AA)	Lattice vector	Value (\AA)
C1	(1.421, 0, 0)	\mathbf{a}_1	(2.1315, -1.2306, 0)
C2	(2.842, 0, 0)	\mathbf{a}_2	(2.1315, -2.1306, 0)
		\mathbf{a}_3	(0, 0, 15.875)

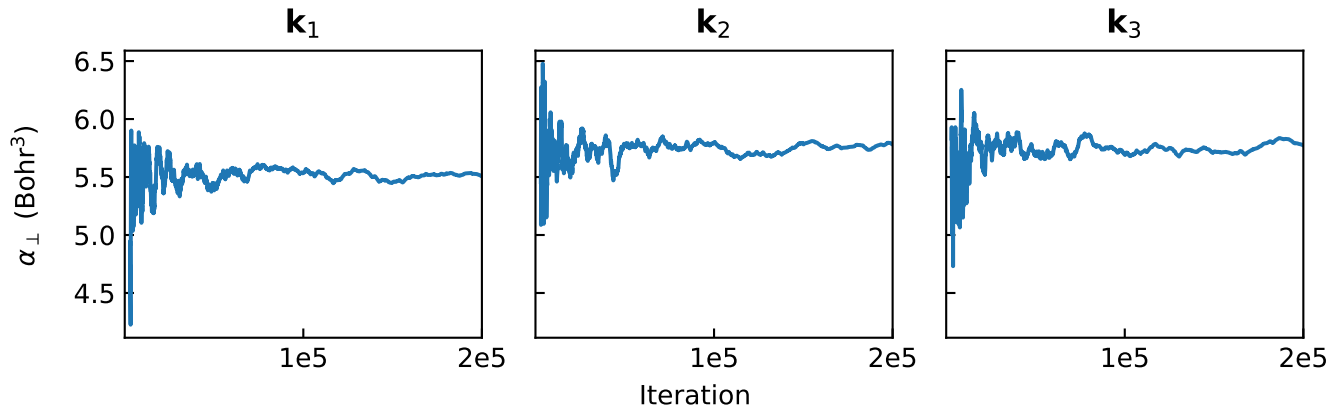


FIG. 6. Training curves of monolayer graphene slab polarizability. For clarity, at each iteration number, we plot the median value of the last 10% of the corresponding iteration.

TABLE XIV. Slab polarizability of graphene.

	\mathbf{k}_1	\mathbf{k}_2	\mathbf{k}_3	Twist average
$\alpha_{\perp}(\text{Bohr}^3)$	5.5(1)	5.7(1)	5.7(1)	5.7(1)

X. BILAYER GRAPHENE

AA-stacked bilayer graphene is chosen for simulation and its geometry is given in Tab XV. And L is set to 3.000\AA , 3.347\AA , and 4.000\AA respectively. Applied electric field is set to $5e-3$ atomic unit. Twist is set to $\mathbf{k}_S = \mathbf{b}_1/3 + \mathbf{b}_2/3$ which has the largest weight in 3×3 twist average. Moreover, the learning rate decay is set to 3 after $2e5$ iterations to reduce fluctuations. Corresponding training curve of polarizability is given in Fig. 7. The calculated polarizability is given in Tab. XVI.

TABLE XV. Geometry of bilayer graphene.

Atom	Position (\AA)	Lattice vector	Value (\AA)
C1	(1.421, 0, $L/2$)	\mathbf{a}_1	(2.1315, -1.2306, 0)
C2	(2.842, 0, $L/2$)	\mathbf{a}_2	(2.1315, -2.1306, 0)
C3	(1.421, 0, $30-L/2$)	\mathbf{a}_3	(0, 0, 15.875)
C4	(2.842, 0, $30-L/2$)		

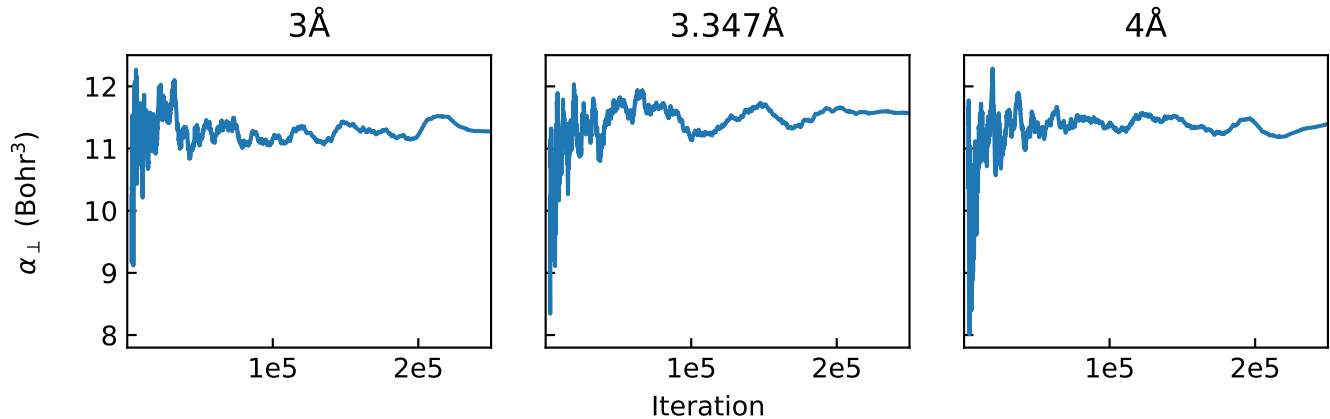


FIG. 7. Training curves of bilayer graphene slab polarizability. For clarity, at each iteration number, we plot the median value of the last 10% of the corresponding iteration.

TABLE XVI. Slab polarizability of bilayer graphene.

$L(\text{\AA})$	3.000	3.347	4.000
$\alpha_{\perp}(\text{Bohr}^3)$	11.3(1)	11.6(1)	11.4(1)

- [1] E. Yu, D. Stewart, and S. Tiwari, Ab initio study of polarizability and induced charge densities in multilayer graphene films, *Physical Review B* **77**, 195406 (2008).
- [2] A. Laturia, M. L. Van de Put, and W. G. Vandenberghe, Dielectric properties of hexagonal boron nitride and transition metal dichalcogenides: from monolayer to bulk, *npj 2D Materials and Applications* **2**, 6 (2018).
- [3] X. Li, Z. Li, and J. Chen, Ab initio calculation of real solids via neural network ansatz, *Nature Communications* **13**, 7895 (2022).
- [4] E. Miliordos and K. L. C. Hunt, Dependence of the multipole moments, static polarizabilities, and static hyperpolarizabilities of the hydrogen molecule on the H–H separation in the ground singlet state, *The Journal of Chemical Physics* **149**, 234103 (2018).
- [5] J. P. Harris, D. R. Manship, W. H. Breckenridge, and T. G. Wright, Comparison of the interactions in the rare gas hydride and Group 2 metal hydride anions, *The Journal of Chemical Physics* **140**, 084304 (2014), https://pubs.aip.org/aip/jcp/article-pdf/doi/10.1063/1.4865749/15472390/084304_1.online.pdf.
- [6] N. E.-B. Kassimi and A. J. Thakkar, Static hyperpolarizability of atomic lithium, *Phys. Rev. A* **50**, 2948 (1994).
- [7] D. Tunega, J. Noga, and W. Klopper, Basis set limit value for the static dipole polarizability of beryllium, *Chemical Physics Letters* **269**, 435 (1997).
- [8] A. K. Das and A. J. Thakkar, Static response properties of second-period atoms: coupled cluster calculations, *Journal of Physics B: Atomic, Molecular and Optical Physics* **31**, 2215 (1998).
- [9] B. Kirtman, V. Lacivita, R. Dovesi, and H. Reis, Electric field polarization in conventional density functional theory: From quasilinear to two-dimensional and three-dimensional extended systems, *The Journal of chemical physics* **135**, 154101 (2011).
- [10] E. F. Archibong and A. J. Thakkar, Chain length dependence of static longitudinal polarizabilities and hyperpolarizabilities in linear polyynes, *The Journal of chemical physics* **98**, 8324 (1993).
- [11] G. Barrera, D. Colognesi, P. Mitchell, and A. Ramirez-Cuesta, Lda or gga? a combined experimental inelastic neutron scattering and ab initio lattice dynamics study of alkali metal hydrides, *Chemical Physics* **317**, 119 (2005), combining Simulations and Neutron Scattering Experiments: from Models to Systems of Biological and Technological Interest.
- [12] E. Staritzky and D. I. Walker, Crystallographic data. 124. lithium hydride, lih; 125. lithium deuteride, lid, *Analytical Chemistry* **28**, 1055 (1956).
- [13] K. Ghandehari, H. Luo, A. L. Ruoff, S. S. Trail, and F. J. DiSalvo, Band gap and index of refraction of csh to 251 gpa, *Solid state communications* **95**, 385 (1995).
- [14] S. S. Batsanov, E. D. Ruchkin, and I. A. Poroshina, *Refractive indices of Solids* (Springer, 2016).